Physics of Fluids

Geometric flow control in lateral flow assays: Macroscopic single-phase modeling

Cite as: Phys. Fluids **34**, 062110 (2022); https://doi.org/10.1063/5.0093316
Submitted: 28 March 2022 • Accepted: 30 May 2022 • Accepted Manuscript Online: 31 May 2022 • Published Online: 15 June 2022

Farshid Jamshidi, Willfried Kunz, Patrick Altschuh, et al.

Physics of Fluids ARTICLE scitation.org/journal/phf

Geometric flow control in lateral flow assays: Macroscopic single-phase modeling

Cite as: Phys. Fluids **34**, 062110 (2022); doi: 10.1063/5.0093316
Submitted: 28 March 2022 · Accepted: 30 May 2022 ·
Published Online: 15 June 2022

Farshid Jamshidi,[1,a)] Willfried Kunz,[1] Patrick Altschuh,[1,2] Marcel Bremerich,[3] Robert Przybylla,[2] Michael Selzer,[1,2] and Britta Nestler[1,2]

AFFILIATIONS

[1]Institute for Digital Materials Research, Karlsruhe University of Applied Sciences, Moltkestraße 30, 76133 Karlsruhe, Germany
[2]Institute for Applied Materials-Microstructure Modelling and Simulation, Karlsruhe Institute of Technology (KIT), Straße am Forum 7, 76131 Karlsruhe, Germany
[3]Sartorius Stedim Biotech GmbH, August-Spindler-Straße 11, 37079 Göttingen, Germany

[a)]Author to whom correspondence should be addressed: farshid.jamshidi@h-ka.de

ABSTRACT

To describe the dynamics of fluid flow in Lateral Flow Assays (LFAs) and to understand the effect of geometry on the propagation speed of the fluid front, a single-phase model is developed. The model can predict wicking time for different geometries. Axisymmetric geometries with changes in their cross sections are studied to understand the wicking behavior. To validate the modeling results, imaging experiments that capture the fluid front are conducted on all geometries. In all cases, convincing agreement between modeling results and experimental data has been observed. Using data-driven information and knowledge about structure–property correlations, it is possible to control wicking processes to establish a desired velocity at a specific position in LFAs. The proposed approach serves as a basis for the creation of a design tool for application-oriented membranes.

I. INTRODUCTION

Rapid Diagnostic Tests (RDTs) are required in medical emergencies or in healthcare facilities with limited resources. One simple and convenient type of RDTs based on antigen detection is the Lateral Flow Assay (LFA).[1] This widespread technology is used to diagnose a range of conditions like pregnancy or infectious diseases, such as COVID-19. LFAs distinguish various types of analytes within a few minutes via color signals on a piece of paper. This paper made from nitrocellulose is a highly porous open-pored membrane. Membranes act in LFAs as the transport medium for the sample fluids (e.g., urine, serum, saliva) where the biochemical reactions occur.

The LFA usually consists of four main components:[2] a sample pad; a conjugate pad; a nitrocellulose membrane on which the test line (TL) and control line (CL) are printed; and an absorbent pad. For easier manufacturing and handling as well as for higher mechanical strength, all these four components are usually assembled on a backing card. The test result is indicated by the accumulation of the stained immunoconjugates at the test and control lines, which is influenced not only by the binding affinity of the reactants but also by the flow rate of the sample.[3] The latter is due to negative capillary pressure, which depends on the interfacial tension between wetting and non-wetting phases as well as the mean curvature in each individual pore.[4,5]

In addition, the wetting behavior is controlled by membrane characteristic values. Algorithms have been developed to characterize membranes on the pore-scale, i.e., microscale in order to determine membrane surface area, porosity, and permeability. These included a spatial generation algorithm for open-pored membranes[6] and methods for reconstructing image data resulting from imaging techniques.[7] Other approaches are required to study the wetting behavior on a larger scale. A comprehensive review of mesoscopic and macroscopic models on wetting in paper-like materials is given in Ref. 8. The focus of this paper is to investigate the flow paths on the macro-scale through membranes with lengths of up to 40 mm. Generally, the penetration of a liquid into a porous medium by capillary suction is referred to as wicking.[9,10] Two conventional approaches to study wicking in rigid open-pored porous media are shortly explained below, and some modifications from the literature to these methods are reported.

The first approach to study wicking in rigid porous media is based on the Hagen–Poiseuille equation by treating the pore space as a bundle of parallel, cylindrical capillary tubes aligned with the flow direction.[11] Bell and Cameron,[12] Lucas,[13] and Washburn[14] studied separately the

movement of liquids through a vertical cylindrical tube due to the wetting of the liquids on the wall. It was concluded that the wicking length is proportional to the square root of the wicking time, which is known as Bell–Cameron–Lucas–Washburn (BCLW) imbibition law.

However, porous media cannot always be regarded as a bundle of circular tubes because in many cases, they are non-circular, tortuous, and even possess complex structures. Therefore, the Hagen–Poiseuille equation and consequently BCLW law are not appropriate to study wicking in most porous materials. This has encouraged many scientists to research the validity of BCLW imbibition law. Berthier *et al.*[15] studied a confined non-circular but uniform cross section and offered a modified prefactor in the usage of BCLW law. The effect of tortuosity in addition to the variably shaped capillary tubes was studied by Cai *et al.*[16] Periodically constricted tubes, such as sinusoidal tubes, were investigated in Refs. 17–19. Reyssat *et al.*[20] demonstrated, experimentally and theoretically, the deviations from BCLW law for geometries with axial variations. They observed that for these kinds of profiles, BCLW law is valid only at short times, whereas at longer times, the wicking length is proportional to the fourth root of the wicking time. Their research was followed by many others.[21–23]

BCLW law describes the capillary-driven liquid flow in porous media only in non-expanding geometries. For expanding porous materials, a potential flow theory in 2D and 3D was proposed in Ref. 24. Well-established BCLW law represents the balance between surface tension and viscosity and neglects fluid inertia and gravity. However, all these four effects are regarded in the model of Liou *et al.*[25] for the capillary rise in axisymmetric tubes. BCLW law disregards the flow effects at the meniscus, which was studied by Mehrabian *et al.*[26] They performed numerical simulations using the finite element method to capture the interface.

The second approach to study wicking in rigid porous media is based on Darcy's law, which correlates the superficial flow velocity to the pressure gradient for a viscous Newtonian fluid at low speed.[27,28] As a side note, the superficial velocity (Darcy velocity) is an artificial velocity calculated in such a way that the porous matrix is disregarded, and the fluid is the only material that flows through the entire cross-sectional area. The interstitial velocity, i.e., the real flow velocity through void spaces between the skeleton, is obtained by dividing the Darcy velocity by the porosity of the media.

Masoodi *et al.*[29] implemented different formulations for the suction pressure in Darcy's law to model liquid absorption in polymer wicks. This led them to two distinct models. The first one is the capillary model in which the suction pressure is equal to the capillary pressure and the second one is the energy balance model in which free surface energy is in balance with the viscous dissipation energy. Considering the effect of gravity, they created two further variants of their models. They showed that the most satisfying results derive from the energy balance model with gravity.

In this paper, an appropriate modeling approach based on Darcy's law is presented to study wicking in nitrocellulose membranes. The aim of this work is to ascertain the influence of membrane shape on the capillary flow using a single-phase approach as well as experimental work. Similar to the study of Shou and Fan,[30] a model for controlling capillary flow in the membranes with varying cross sections is presented here. They studied imbibition in homogeneous porous structures on the macro-scale and could find the optimal geometry for the fastest (slowest) imbibition based on a computational approach. However, the mathematical equation presented in this work describes the wicking process in membranes with any desired shape. The remainder of this paper is organized as follows. In Sec. II, the case studies are introduced and the mathematical framework of the single-phase approach together with the experimental procedure is described. The results of this study are presented in Sec. III. Finally, Sec. IV summarizes the main conclusions of the work.

II. MATERIALS AND METHODS

A. Porous membranes

In a lateral flow assay, the analyte moves through the membrane by the capillary flow (convection), diffuses toward the capture zones (diffusion), and builds a complex with antibodies (reaction). Each of these three phenomena has a characteristic timescale as follows:[3]

1. Convection: The residence time is defined as $t_R = w_{TL}/u_{TL}$, where w_{TL} is the width of the test line (TL) and u_{TL} is the wicking velocity through the TL. The wicking velocity decreases along the membrane but because the TL width is much smaller than the TL position ($w_{TL} \ll X_{TL}$), u_{TL} can be assumed constant [see Fig. 1(a)].

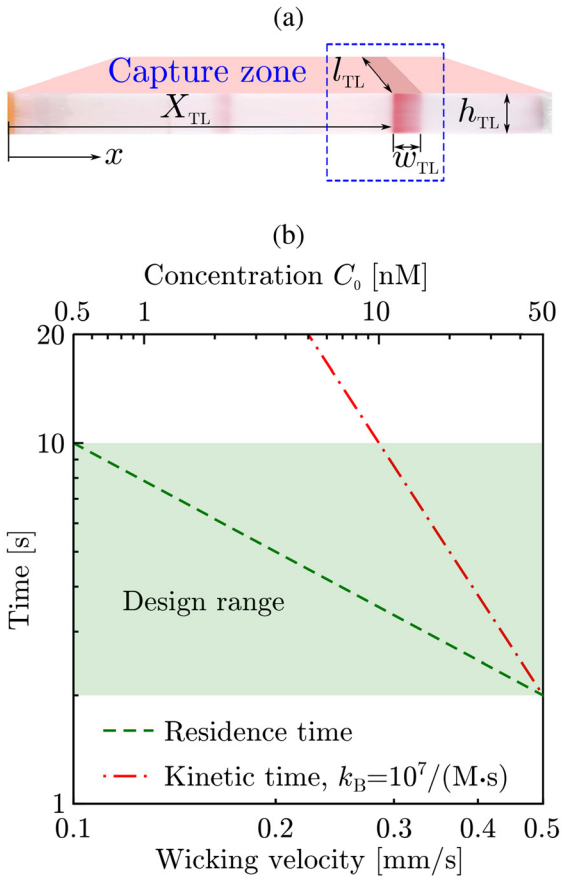

FIG. 1. (a) Schematic representation of a lateral flow assay and its test line as the capture zone; (b) residence time as a function of the wicking velocity and characteristic kinetic time as a function of analyte concentration for a binding affinity of 10^7/(M s).

TABLE I. Parameters for calculating different timescales in LFAs.

Parameter	Value
Width of the test line: w_{TL}	1 mm (Ref. 3)
Diffusion coefficient: D	20–2000 $\mu m^2/s$ (Ref. 31)
Wicking velocity: u_{TL}	0.1–0.5 mm/s (Ref. 32)
Binding constant: k_B	10^4–10^7/(M s) (Ref. 32)
Mean pore diameter: d_P	3.74 μm (Ref. 7)
Initial concentration: C_0	0.5–50 nM (Ref. 33)

2. Diffusion: The term diffusive time refers to $t_D = d_P^2/D$, where d_P is the mean pore size of the membrane and D is the molecular diffusion coefficient.
3. Reaction: The characteristic kinetic time is $t_K = 1/(k_B \cdot C_0)$, where k_B represents the binding constant and C_0 is the analyte concentration.

Calculating the timescales of these three phenomena and comparing them specify a time interval in which all of them can occur. To do so, the parameters for LFAs from Table I are used.

The results show that the diffusive time is shorter than the residence and kinetic times ($2\,s \le t_R \le 10\,s$; $0.007\,s \le t_D \le 0.7\,s$; $2\,s \le t_K \le 2 \times 10^5\,s$). In other words, the molecular diffusion happens much faster than convection and reaction. Therefore, to define a design range, it is necessary to pay attention to convection and reaction. Figure 1(b) shows both the dependence of the residence time on the wicking velocity through TL and the dependence of the characteristic kinetic time on the analyte concentration for the binding constant $k_B = 10^7/(M\,s)$. Other binding affinities are not in the plot range, so they are not illustrated here. The intersection of the residence and kinetic times can be taken as the design range.

The focus of this work should lie on the residence time. By varying the geometry of the membrane, the wicking velocity through the test line changes, and this leads to a new residence time. Thus, it is important to know how the shape of a membrane influences the wicking velocity. The membrane profiles studied in this work are illustrated in Fig. 2 and labeled as straight, barbell, hexagon, sand timer, and T-shaped channels. The membrane itself is a UniSart® CN 140 backed, which is a nitrocellulose membrane reinforced by a polyester film for lateral flow immunoassays and commercially available (Sartorius Stedim Biotech GmbH, Germany) with an average thickness of 240 μm, and it takes between 95 and 155 s for purified water as the sample liquid to travel a distance of 40 mm of this membrane as specified by the manufacturer.

B. Mathematical modeling

Mathematical modeling of liquid transport in porous media creates a theoretical groundwork for optimizing (controlling) the wicking process. For instance, it is possible to reach a desired flow velocity in a specific location like at the TL/CL or to obtain the fastest imbibition.[34] Therefore, modeling the capillary-driven flow through a membrane with different shapes is carried out by extending the models of Refs. 35 and 36. Elizade *et al.*[35] investigated the capillary imbibition in paper-based membranes on the macro-scale. They offered a mathematical solution to determine the wicking time for an arbitrary cross-sectional profile. Their method also allowed them to solve the inverse problem, i.e., to find the shape required for a prescribed fluid velocity. In the presence of different segments, Shou *et al.*[36] explored the effect of width and length of local segments on the capillary motion. In this paper, we combine their methodologies and generalize their equations to obtain the wicking time t for our membranes. The direction of the flow is shown as x or z in Fig. 2. The wicking times for the first, second, and third segments of the different geometry profiles are denoted by t_1, t_2, and t_3, respectively, and can be written as follows (for more detailed information, the reader is referred to Appendix A):

$$t_1 = \zeta \int_0^l a_1(z) \left[\int_0^z \frac{dx}{a_1(x)} \right] dz, \tag{1a}$$

$$t_2 = \zeta \int_{h_1}^l a_2(z) \left[\int_0^{h_1} \frac{dx}{a_1(x)} + \int_{h_1}^z \frac{dx}{a_2(x)} \right] dz, \tag{1b}$$

$$t_3 = \zeta \int_{h_1+h_2}^l a_3(z) \left[\int_0^{h_1} \frac{dx}{a_1(x)} + \int_{h_1}^{h_1+h_2} \frac{dx}{a_2(x)} + \int_{h_1+h_2}^z \frac{dx}{a_3(x)} \right] dz, \tag{1c}$$

where l denotes the position of the fluid front, and h_i and a_i are the length and width of each individual segment ($i = 1, 2, 3$), respectively. In the case of geometries with only two segments, e.g., the hexagon profile, Eq. (1c) is omitted. The coefficient ζ considers the influence of the dynamic viscosity μ, the permeability K, and the capillary pressure Δp_c as well as the reinforcement. The effect of gravity is neglected here as the Bond number is much less than one ($Bo \ll 1$, see Appendix B).

We set $H_n = \sum_{i=0}^n h_i$ as the sum of the length of n layers, where $H_0 = h_0 = 0$, then the wicking time for the nth layer can be written as

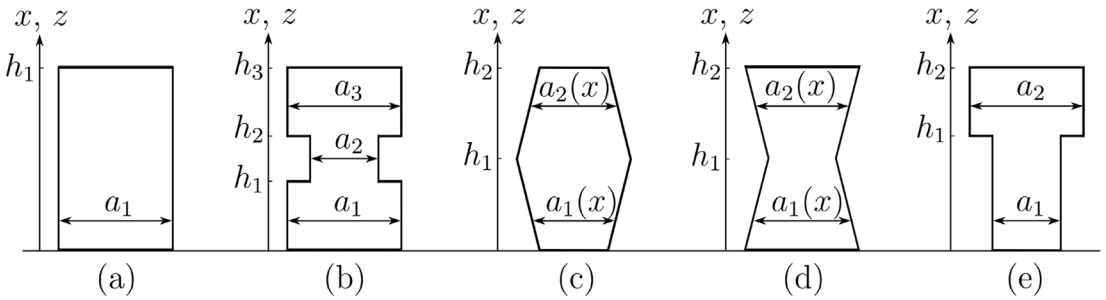

FIG. 2. Sketch of membrane profiles: (a) straight, (b) barbell, (c) hexagon, (d) sand timer, and (e) T-shaped membrane.

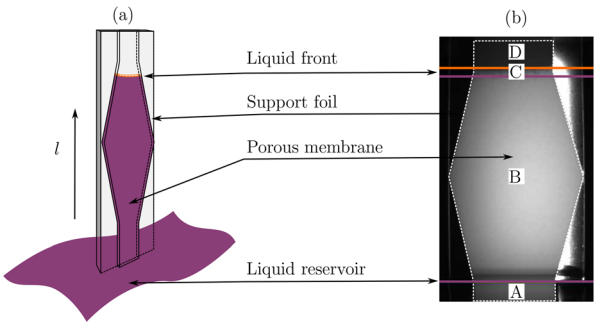

FIG. 3. (a) Schematic of the wicking experiment and (b) a real image of the detection of the liquid front during the experiment.

$$t_n = \zeta \int_{H_{n-1}}^{l} a_n(z) \left[\left(\sum_{i=1}^{n-1} \int_{H_{i-1}}^{H_i} \frac{dx}{a_i(x)} \right) + \int_{H_{n-1}}^{z} \frac{dx}{a_n(x)} \right] dz. \quad (2)$$

Using this method, it is possible to predict the wicking time for a membrane including multiple segments with arbitrary cross sections. One benefit of this methodology is the simplicity over other methods that require applying a mesh and numerically solving differential equations. The only challenge is to find the coefficient ζ, which is determined in this work from the experimental wicking curve of a straight channel. For the straight membrane, BCLW imbibition law ($t = \frac{1}{2}\zeta l^2$) is fitted to experimental data using Gnuplot 5.0 patchlevel 5[37] to gain the coefficient ζ. This coefficient is used for the other types of profiles sketched in Fig. 2.

C. Wicking experiment

Wicking experiments are commonly conducted directly after the production process for quality control of membranes or their classification. The time spent on wetting the entire length of a piece of membrane is called the total wicking time T_w while the curve progression of wicking length over time reveals the characteristic wicking behavior. A standardized experimental approach is presented to gain wicking curves for the membranes with the profiles exhibited in Figs. 2(a)–2(d). The desired profiles in this study have larger widths than the critical width of the membrane CN 140 [600 μm (Ref. 38)]. It means that the widths of the profiles do not influence the wicking process, and there are no boundary effects. Under this circumstance, the membrane samples were first cut into the desired profiles; then, the two shorter edges of the membranes (top and bottom) were clamped firmly onto a rectangular plastic frame. Thus, the paper-based membranes were kept in a flat and stable position without bending. Then, the frame was inserted into the basin of a custom-made device, in particular designed to measure the wicking time. At the bottom of the basin, a thin film of the test liquid (here: water) existed.

As soon as the frame touched the bottom of the device, water commenced to wick the membrane and a camera took one photo per second of the front side of the membrane. The membrane was illuminated by an LED from the back side. Custom-written algorithms were used to extract the propagating liquid front (l) over time by detecting the difference in contrast between the dry and wetted membrane. By the membrane with a width of 5 mm, too much light came from the light source, passed the membrane and, hence, caused overexposed photos. Therefore, 15 mm was set as the minimum threshold for the membrane width. On the other hand, the maximum width of 25 mm and the maximum length of 40 mm were selected due to size restrictions of the custom-made device. To ensure repeatability, the test for each profile was performed six times.

Figure 3(a) shows schematically a membrane during wicking by a magenta liquid while in Fig. 3(b), the actual membrane is shown and divided into four regions. In region A, the membrane is in contact with a liquid reservoir, so that enough liquid is available to wet the entire membrane. In region B, the membrane is fully saturated with the liquid and its length is taken as the wicking length (between the magenta lines). The border of regions B and C is supposed to be the liquid front in this work. A kind of "mushy" region with partially wetted and partially dry surface areas is observed in region C, while in region D, the membrane is completely dry. The border between regions C and D (orange line) was called the precursor of impregnation by Bico and Quéré.[39]

Since a porous medium has often been treated as a bundle of parallel identical tubes (as by BCLW imbibition law), the fluid front is modeled as a sharp interface; however, it is diffuse in reality. Bico and Quéré[39] modeled the pore space as two interconnected cylindrical capillary tubes with different radii. In their model, the fluid moves faster through the tube with the smaller radius, while more fluid mass exists in the tube with the larger radius. By validating the model with experimental data, they declared that the fluid front is diffusive [region C in Fig. 3(b)].

In addition to the experiments with the straight, barbell, hexagon, and sand timer profiles using the aforementioned measuring device [Figs. 4(a)–4(d)], two videos of experiments with the T-shaped

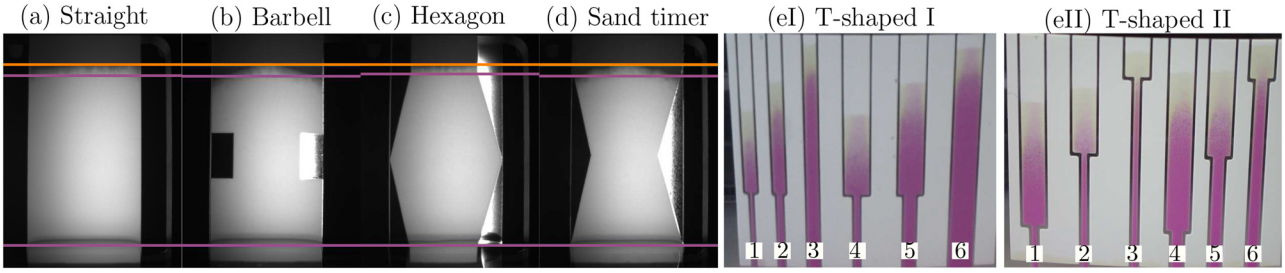

FIG. 4. Wicking experiments using different membrane profiles, where (a)–(d) membranes are fully saturated between the magenta lines and are totally dry above the orange lines; (eI) and (eII) phenol red was added into the liquid (water) for better visualization of the wicking process in samples 1–6.

membranes were provided by Sartorius Stedim Biotech GmbH, Germany [Figs. 4(eI) and (eII)]. For better observation and analysis of the wicking process, phenol red as the coloring agent was beforehand added into the liquid and a camera recorded the video. From the video, one frame per second was captured as an image. The image sequence was imported to `Fiji-ImageJ 1.53c`[40] and processed using the tool `ColorThreshold`. The most superior colored pixel was tracked to distinguish the liquid front.

III. RESULTS AND DISCUSSION

A. Straight, barbell, hexagon, and sand timer membranes

The results of the single-phase approach are compared to experimental data for distinct geometries in Fig. 5, where the time-dependent position of the liquid front l during wetting is shown. As stated before, the coefficient ζ in Eq. (1) is obtained by fitting BCLW law with the experimental data of the straight membrane [Fig. 5(a)] and used for modeling the wicking process of the other three profiles. In comparison with the straight test strip as a reference, changes in the cross-sectional area influence the movement of the liquid front. The single-phase approach can capture this influence and predict the wicking time for the channels composed of different segments with constant widths (barbell) as well as with varying widths (hexagon and sand timer).

The barbell membrane is composed of three straight segments. For each segment, there exists a wicking function. Because the second segment has a smaller width, the wicking velocity increases and afterward by entering the third segment, the fluid flows more slowly. In comparison with the flow through the membrane with the barbell

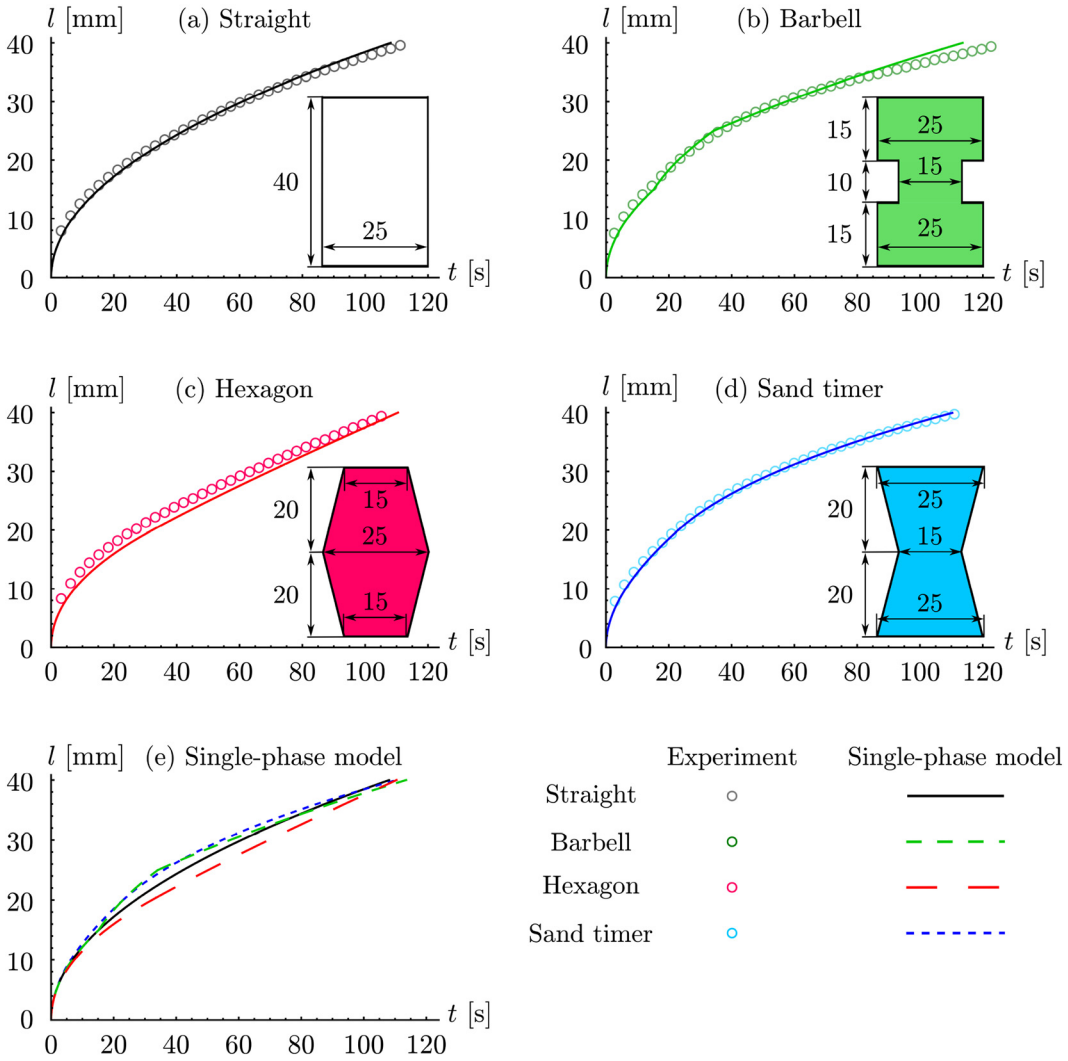

FIG. 5. The position of the meniscus over time by the single-phase approach and experiment for the (a) straight, (b) barbell, (c) hexagon, and (d) sand timer profiles; and (e) the results of single-phase method are shown for all the profiles. The inset figures show the dimensions of each profile in mm. For better visualization, the results of the model are illustrated by solid lines in (b)–(d).

profile, the single-phase model shows a smoother movement of the fluid in the hexagon and sand timer profiles. As can be seen in Fig. 5(e), the flow in the first segment of the hexagon profile (diverging segment) moves more slowly than that of in the first segment of the sand timer profile (converging segment). This can also be observed in the second segment of the sand timer profile.

In general, the model shows a good agreement with experimental observations. In conclusion, the capillary flow velocity increases by narrowing and decreases by widening.

In order to conduct a design study and to broaden knowledge about the influence of converging and diverging segments of the hexagon and sand timer profiles on the wicking behavior, nondimensionalization is applied by selecting the total wicking time of the straight test strip as the scale. For this purpose, t_1 from Eq. (1a) and t_2 from Eq. (1b) are divided by $T_{\text{Straight}} = \frac{1}{2}\zeta H^2$. The dimensionless time is plotted over the ratio of the wicking length to the total membrane length in Fig. 6(a). The gray line represents the wicking time of the straight membrane. The red and blue curves belong to the hexagon and sand timer profiles, respectively. In the legend, the schematic of the profiles and the ratio between the lengths of the first segment and the entire membrane h_1/H are shown. The diagram illustrates the same termination point if the diverging (or converging) parts of the hexagon and sand timer profiles have the same length; in other words, only the length of each segment affects the final wicking time, not the arrangement of the diverging and converging parts. In addition to the dimensionless time, its derivative is also depicted in Fig. 6(b) to highlight the changes in the wicking time. It can be seen that the slope of each curve changes at the cross-sectional change. The larger the slope of this diagram is, the lower the wicking velocity is. Thus, by using this diagram, the influence of shapes on the capillary flow velocity can be estimated. It becomes once again clear that the wetting speed decreases through diverging parts and increases through converging parts.

Furthermore, the diagram directly demonstrates how to reach the required flow velocity in the test and control line regions by modifying the length of each segment. The diagram is independent of the material of the membrane, interfaces, and liquid properties, since all channel shapes are compared to the unstructured test strip as a reference.

One of the design criteria of LFAs is the wicking velocity at the test line (TL). At $l/H \approx 0.7$, the wicking velocities through the hexagon and sand timer profiles with $h_1/H = 0.5$ are almost the same as that of the straight membrane. Thus, if the TL is inserted in the membrane at 0.7 of the total length, despite the same wicking velocity, the wicking time is much less for the sand timer profile.

By inserting the TL at $l/H = 0.8$ for all h_1/H, the fluid passes through the cross-sectional change in the hexagon and sand timer profiles. It is observed that for all these profiles with the total length of 40 mm, the smallest width of 15 mm, and the largest width of 25 mm, the wicking velocity lies within the range of LFA velocities[32] and consequently with the TL width of 1 mm, the residence time is in the design range [see Fig. 1(b)].

Erickson *et al.*[41] performed numerical simulations using the finite element method to see the wetting behavior of converging–diverging and diverging–converging capillaries. In contrast to the present work, a straight section separated the converging and diverging parts in their simulations and they did not study porous media; however, their results confirmed the findings here. In both works, the driving force of the flow is the capillary force and the resistance force to flow is the viscous force.

B. T-shaped membranes

The experiment with the T-shaped membranes I [Fig. 4(eI)] was conducted to investigate the influence of the sudden change in width but on the same length. Moreover, the cross-sectional changes in length were studied using T-shaped membranes II [Fig. 4(eII)]. Figures 7 and 8 show the individual liquid rises through the T-shaped membranes over time. The points represent experimental data, while solid curves in the same color depict the corresponding data from the single-phase model represented in Sec. II B. From all the membranes, only the samples 3 and 6 in Fig. 7 [Fig. 4(eI)] possess the straight profile. Thus, by fitting with experimental data from these two samples, i.e., using their arithmetic average, the coefficient ζ [in Eq. (A6)] was determined.

The model shows a good agreement with experimental data in Fig. 7. Although the straight samples 3 and 6 have different widths

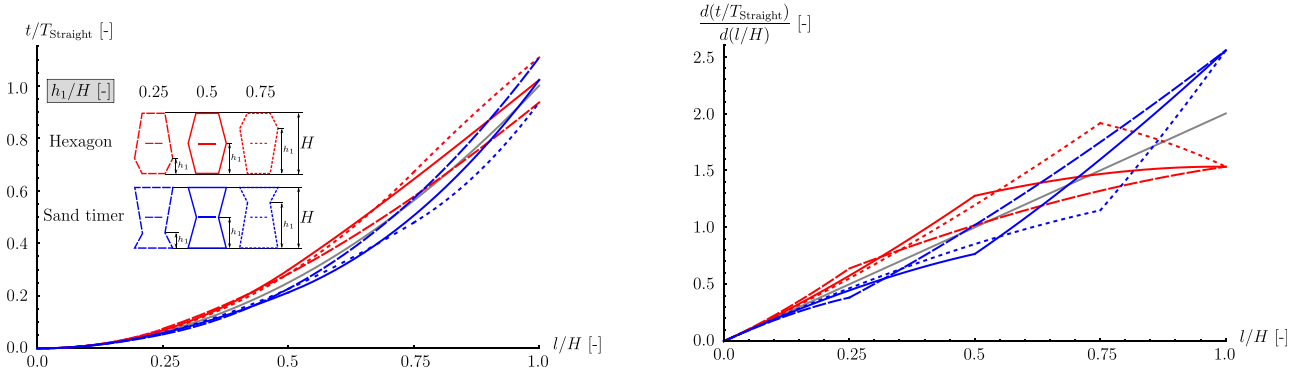

FIG. 6. (a) The dimensionless wicking time and (b) its derivative for the hexagon and sand timer profiles by comparison with the straight membrane (shown by the gray line).

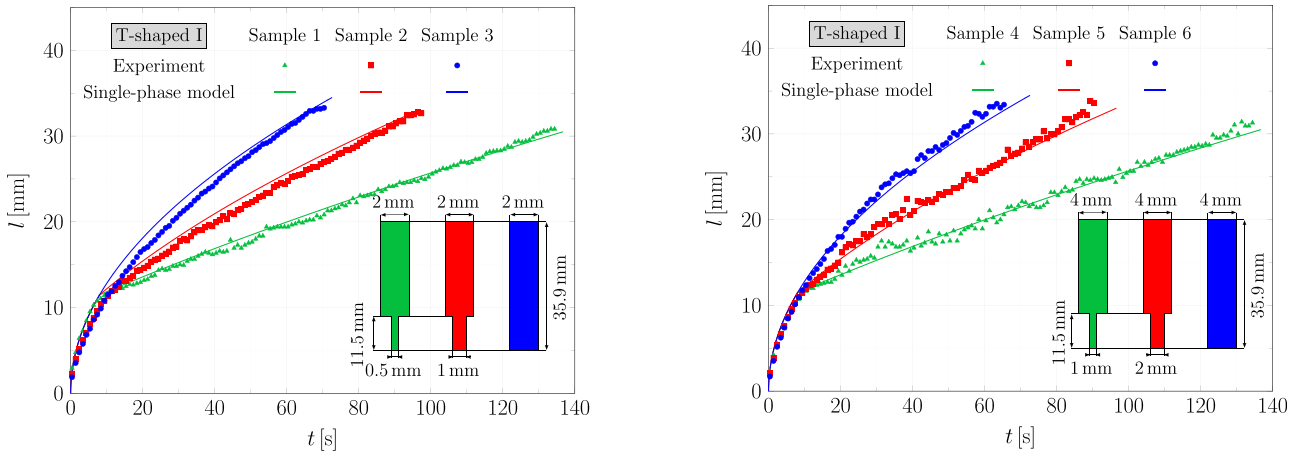

FIG. 7. The wicking length over time in the T-shaped membranes I for (a) samples 1–3 and (b) samples 4–6.

(2 and 4 mm, respectively), they show almost the same wicking behavior, as they are identical in the mean pore radius. For the membrane CN 140, Hecht *et al.*[38] found that the critical width of the channel is 600 μm above which the wicking velocity does not depend on the width. Hong and Kim also studied the wicking process in straight membranes with cut and wax boundaries and found that the wicking velocity is not influenced by the channel width in the case of cut boundaries.[42] Since the membranes in this work have cut boundaries (not wax) and the widths of samples 3 and 6 are both larger than the critical value, they have the same wicking velocity. For the other samples, it can be seen that expansion leads to velocity reduction in the subsequent segment along which the wicking velocity is almost constant.[43]

As explained in Ref. 36, it is hard for a thinner segment to provide enough liquid for the wider membrane. In other words, the source can hardly cover the increasing demand for fluid and, therefore, the fluid requires more time to propagate in the wider cross section. On the other hand, it can be seen that the flow resistance decreases with the falling width ratio and the fluid finds its final position faster when no expansion occurs.

Figure 8 shows how the changes in cross section in different lengths influence the wicking time. The length ratios are the same for samples 1 and 4; 2 and 5; and 3 and 6, respectively, while the width ratios are 4 for samples 1–3 and 2 for samples 4–6.

As can be seen in Fig. 8(a), the sooner the liquid enters the second segment, the larger the slope of the wicking length, i.e., the higher the liquid velocity in this segment is. Specifically, the wicking velocity of sample 1 in its second segment (green line) is larger than that of sample 2 (red line) and consequently the fluid front of sample 1 overtakes that of sample 2. Thus, the entire wicking proceeds more slowly

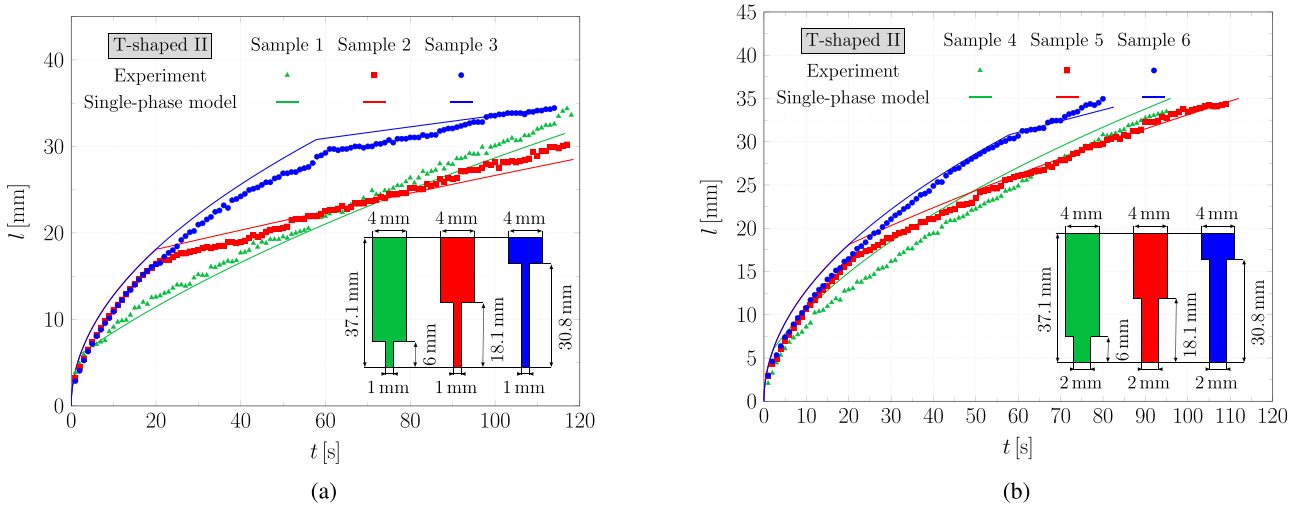

FIG. 8. The wicking length over time in the T-shaped membranes II for (a) samples 1–3 and (b) samples 4–6.

in sample 2 in comparison with sample 1. A faster imbibition rate for a membrane with a shorter narrow segment (sample 1 as compared to sample 2) was also observed by Tirapu-Azpiroz *et al.*[43] Contrarily, Fu *et al.*[44] described that the liquid front has the largest transport time for the shortest first segment (sample 1). They used a shorter time interval in which the front of sample 1 could not yet reach its final position and could not overtake the liquid front of sample 2.

By lengthening the first segment, the liquid source becomes more limited for the second segment and the flow resistance increases in the second segment and, hence, the fluid spreads more slowly in this segment. Thus, the flow velocity is the lowest in the second segment of sample 3. Nevertheless, the total wicking time of sample 3 is the shortest. The expansion of sample 3 happens later than samples 1 and 2, and the fluid can flow faster in a longer straight channel (30.8 mm).

The same interpretation applies to Fig. 8(b) where the liquid front of sample 4 overtakes that of sample 5 but not that of sample 6. The only difference with samples 1–3 is that the first segment is wider. This allows a larger flow rate through the first segment, and the problem of the limiting source for the second segment is, thus, reduced. Therefore, the changes in the slope of the liquid propagation between the first and second segments of samples 4–6 are not so large as those of samples 1–3, respectively.

It is worth mentioning that the coefficient ζ is deduced from the wicking process of the straight membranes in the experiment with the T-shaped membrane I. Thus, the larger deviation between the experimental and modeling results for the T-shaped membrane II (in particular for sample 4) can be explained by errors associated with the transfer of the constant ζ from the separate video with a different zoom and exposure value. An additional reason for this deviation of sample 4 was the difficulty by determining the liquid front as the front with approximately 100% saturation.

In a nutshell, the expansion in the different membrane profiles reduces the wicking velocity and all the slopes of the liquid propagation in the second segments are less than that of the straight membrane.

IV. CONCLUSION

On the macro-scale, a single-phase model for liquid transport in lateral flow assays is developed, and experimental studies are conducted to validate this model. The aim of this work is to understand how geometrical changes in the membrane profile influence on the wicking process, and hence, the parameters related to the membrane, such as permeability, or related to the liquid, such as viscosity, are not of interest. Their influences are considered by fitting BCLW law with the experimental data of the straight membrane. Be of interest, different geometries are chosen as the membrane profiles, from straight, barbell, hexagon, and sand timer to T-shaped membranes. This permits understanding of the wicking behavior in paper-based membranes including cross-sectional changes.

By the same beginning and end wicking widths, if the half of the membrane profile or more is diverging, such as in a hexagon or sand timer, the wicking time is longer than that of the straight membrane. Conversely, if the membrane has a converging segment by more than half of its length, the wicking time decreases. The lengths of diverging and converging segments directly influence the wicking time, not their orders (being the first or second segment).

Similar to the diverging segment, an expansion in the T-shaped membranes slows down the wicking process compared to that of the straight membrane. Moreover, in Ref. 36, it is shown that the expansion in the middle of the membrane length causes the slowest wicking. In comparison with this length for an expansion, it is illustrated here that the expansion below this length causes a higher velocity in the second segment, which allows a faster wicking. Furthermore, by increasing the width ratio of an expansion, the wicking velocity decreases.

BCLW imbibition law cannot calculate the wicking time in multi-layer membranes. However, Eq. (2) can determine the wicking behavior of any type of membrane profile. By conducting one single wicking experiment using a straight membrane to discover the wicking coefficient (ζ) and by applying this equation, one can predict the wicking behavior in membranes with non-straight geometries. This prevents time-consuming experiments and saves money. By knowing the effect of the membrane profile on the wicking process, one can control it. Hence, it is possible to reach a desired velocity at the test line considering the residence time; this is essential to improve the test sensitivity and optimize the design of a profile to reduce the time required to deliver the same result. The findings can be used to develop a simulation-based and data-driven membrane design tool that provides the optimum parameters in terms of membrane structure, the wicking time, and signal line position for different test applications.

ACKNOWLEDGMENTS

This work was supported in part by the German government through the BMBF (Bundesministerium fur Bildung, Forschung und Technologie) project OptiProt (Project No. 13FH044PX5) and in part by the Ministry of Science, Research and Art Baden-Württemberg (MWK-BW) in the project MoMaF—Science Data Center, with funds from the state digitization strategy digital@bw (Project No. 57). The second author acknowledges the financial support and thanks for providing experimental data from Sartorius Stedim Biotech GmbH in Göttingen, Germany.

AUTHOR DECLARATIONS

Conflict of Interest

The authors have no conflicts to disclose.

DATA AVAILABILITY

The software packages `Mathematica 11.3`[45] and `Fiji-ImageJ 1.53c`[40] were used for the generation of the data sets. For data management, `Kadi4Mat` as a research data infrastructure for materials science[46] was used. The data that support the findings of this study are openly available in Zenodo from `Kadi4Mat` at https://doi.org/10.5281/zenodo.6389659, Ref. 47.

APPENDIX A: WICKING TIME

The mathematical derivation of Eqs. (1a)–(1c) is presented here. When the fluid front is in the first segment ($z \leq h_1$) with the volumetric flow rate of Q and the cross-sectional area of $A_1(x)$, the Darcy equation can be written as[36]

$$Q = u_1(x)A_1(x) = -\frac{K}{\mu}\frac{dp}{dx}A_1(x). \tag{A1}$$

By integrating Eq. (A1), we obtain

$$\int_{p_0}^{p_1} dp = -\frac{\mu Q}{K}\int_0^z \frac{dx}{A_1(x)}, \tag{A2}$$

where the negative of the rhs represents the liquid pressure drop in the first segment $\Delta p_{01} = p_0 - p_1$, which is equal to the capillary pressure Δp_c and, therefore, we can write

$$\Delta p_c = \frac{\mu Q}{K}\int_0^z \frac{dx}{A_1(x)}. \tag{A3}$$

Considering $Q = u_1(z)A_1(z)$ and $u_1(z) = dz/dt$, we can derive the wicking time for the first segment as t_1

$$\Delta p_c = \frac{\mu}{K}\frac{dz}{dt}A_1(z)\int_0^z \frac{dx}{A_1(x)}, \tag{A4}$$

$$t_1 = \frac{\mu}{K\Delta p_c}\int_0^l A_1(z)\left[\int_0^z \frac{dx}{A_1(x)}\right]dz. \tag{A5}$$

If $A_1(x) = a_1 \cdot b =$ constant, where a_1 and b are the width and thickness of the membrane, respectively, then the wicking time for a straight channel is the same as the result of BCLW imbibition law

$$t_1 = \zeta\int_0^l a_1 \cdot b\left[\int_0^z \frac{dx}{a_1 \cdot b}\right]dz = \frac{1}{2}\zeta l^2, \tag{A6}$$

where $\zeta = \mu/(K\Delta p_c)$. In our study, ζ is constant and obtained by fitting the results to experimental data of the straight channel.

When the liquid front is in the second segment ($h_1 < z \le h_2$), the pressure drop is the sum of pressure drops of the entire first segment and the part of second segment wetted by the liquid, which is equal to the capillary pressure

$$\Delta p_c = \frac{\mu Q}{K}\int_0^{h_1} \frac{dx}{A_1(x)} + \frac{\mu Q}{K}\int_{h_1}^z \frac{dx}{A_2(x)}. \tag{A7}$$

Considering $Q = u_2(z)A_2(z)$ and $u_2(z) = dz/dt$, we can rewrite Eq. (A7) in order to derive the wicking time for the second segment t_2 as follows:

$$\Delta p_c = \frac{\mu}{K}\frac{dz}{dt}A_2(z)\left[\int_0^{h_1} \frac{dx}{A_1(x)} + \int_{h_1}^z \frac{dx}{A_2(x)}\right], \tag{A8}$$

$$t_2 = \frac{\mu}{K\Delta p_c}\int_{h_1}^l A_2(z)\left[\int_0^{h_1} \frac{dx}{A_1(x)} + \int_{h_1}^z \frac{dx}{A_2(x)}\right]dz, \tag{A9}$$

and analog for the third segment

$$t_3 = \frac{\mu}{K\Delta p_c}\int_{h_1+h_2}^l A_3(z)\left[\int_0^{h_1} \frac{dx}{A_1(x)} + \int_{h_1}^{h_1+h_2} \frac{dx}{A_2(x)} + \int_{h_1+h_2}^z \frac{dx}{A_3(x)}\right]dz. \tag{A10}$$

In our study, the thickness remains constant for all segments. Thus, the aforementioned equations for the wicking time are written in Eqs. (1a)–(1c) as functions of the width of segments, namely, $a_1(x)$, $a_2(x)$, and $a_3(x)$. It is again worth mentioning that ζ is obtained from experimental data.

APPENDIX B: BOND NUMBER

The Bond number is a dimensionless number that represents the ratio of gravitational to capillary forces and is defined as[48]

$$Bo = \frac{\rho_L \cdot g \cdot H}{2 \cdot \sigma_{LG}/R}, \tag{B1}$$

where indices L and G stand for the liquid and gas, respectively, ρ_L is the liquid density, g is the gravitational acceleration, H is the total wicking length, σ_{LG} is the coefficient of surface tension between the liquid and gas phases, and R is the capillary radius.

In this study, the liquid phase is water and the gas phase is air. Thus, $\rho_L = 998\ \mathrm{g/m^3}$ and $\sigma_{LG} = 0.073\ \mathrm{N/m}$ at 20 °C, $g = 9.8\ \mathrm{m/s^2}$,[49] $H = 0.04$ m and the mean pore radius (the half of mean pore diameter from Table I[7]) is taken as the capillary radius $R = 1.87\ \mu$m. By using these parameters in Eq. (B1), the Bond number is equal to 0.004 77, to put it another way, $Bo \ll 1$. Thus, the gravitational force is much less than the capillary force and can be neglected in this work. Although the membranes are located vertically, the influence of gravity can be ignored. In many practical conditions, where LFAs locate horizontally, this effect is also negligible. For more information about avoiding (considering) the effect of gravity, the reader is referred to Ref. 50.

REFERENCES

[1] M. M. Gong and D. Sinton, "Turning the page: Advancing paper-based microfluidics for broad diagnostic application," Chem. Rev. **117**, 8447 (2017).
[2] E. B. Bahadır and M. K. Sezgintürk, "Lateral flow assays: Principles, designs and labels," TrAC Trends Anal. Chem. **82**, 286 (2016).
[3] C. L. A. Berli and P. A. Kler, "A quantitative model for lateral flow assays," Microfluid. Nanofluid. **20**, 104 (2016).
[4] R. T. Armstrong, M. L. Porter, and D. Wildenschild, "Linking pore-scale interfacial curvature to column-scale capillary pressure," Adv. Water Resour. **46**, 55 (2012).
[5] J. E. McClure, S. Berg, and R. T. Armstrong, "Capillary fluctuations and energy dynamics for flow in porous media," Phys. Fluids **33**, 083323 (2021).
[6] P. Altschuh, Y. C. Yabansu, J. Hötzer, M. Selzer, B. Nestler, and S. R. Kalidindi, "Data science approaches for microstructure quantification and feature identification in porous membranes," J. Membr. Sci. **540**, 88 (2017).
[7] A. Ley, P. Altschuh, V. Thom, M. Selzer, B. Nestler, and P. Vana, "Characterization of a macro porous polymer membrane at micron-scale by confocal-laser-scanning microscopy and 3D image analysis," J. Membr. Sci. **564**, 543 (2018).
[8] L. Zhi, H. Xiaocong, H. Jiaxiu, Z. Xiuhai, L. Fei, L. Ang, Q. Zhiguo, and X. Feng, "Liquid wicking behavior in paper-like materials: Mathematical models and their emerging biomedical applications," Microfluid. Nanofluid. **22**, 132 (2018).
[9] R. Masoodi and K. M. Pillai, *Wicking in Porous Materials: Traditional and Modern Modeling Approaches* (CRC Press, 2012), p. 380.
[10] J. Kim, M.-W. Moon, and H.-Y. Kim, "Capillary rise in superhydrophilic rough channels," Phys. Fluids **32**, 032105 (2020).
[11] M. A. F. Zarandi, K. M. Pillai, and A. S. Kimmel, "Spontaneous imbibition of liquids in glass-fiber wicks. Part I: Usefulness of a sharp-front approach," AIChE J. **64**, 294 (2018).
[12] J. M. Bell and F. K. Cameron, "The flow of liquids through capillary spaces," J. Phys. Chem. **10**, 658 (1906).
[13] R. Lucas, "Ueber das Zeitgesetz des kapillaren Aufstiegs von Flüssigkeiten," Kolloidn.-Z. **23**, 15 (1918).
[14] E. W. Washburn, "The dynamics of capillary flow," Phys. Rev. **17**, 273 (1921).
[15] J. Berthier, D. Gosselin, and E. Berthier, "A generalization of the Lucas–Washburn–Rideal law to composite microchannels of arbitrary cross section," Microfluid. Nanofluid. **19**, 497 (2015).

[16]J. Cai, E. Perfect, C.-L. Cheng, and X. Hu, "Generalized modeling of spontaneous imbibition based on Hagen–Poiseuille flow in tortuous capillaries with variably shaped apertures," Langmuir **30**, 5142 (2014).
[17]R. Sharma and D. S. Ross, "Kinetics of liquid penetration into periodically constricted capillaries," J. Chem. Soc., Faraday Trans. **87**, 619 (1991).
[18]T. L. Staples and D. G. Shaffer, "Wicking flow in irregular capillaries," Colloids Surf., A **204**, 239 (2002).
[19]D. Patro, S. Bhattacharyya, and V. Jayaram, "Flow kinetics in porous ceramics: Understanding with non-uniform capillary models," J. Am. Ceram. Soc. **90**, 3040 (2007).
[20]M. Reyssat, L. Courbin, E. Reyssat, and H. A. Stone, "Imbibition in geometries with axial variations," J. Fluid Mech. **615**, 335–344 (2008).
[21]J.-B. Gorce, I. J. Hewitt, and D. Vella, "Capillary imbibition into converging tubes: Beating Washburn's law and the optimal imbibition of liquids," Langmuir **32**, 1560 (2016).
[22]L. Courbin, J. C. Bird, M. Reyssat, and H. A. Stone, "Dynamics of wetting: From inertial spreading to viscous imbibition," J. Phys.: Condens. Matter **21**, 464127 (2009).
[23]A. Budaraju, J. Phirani, S. Kondaraju, and S. S. Bahga, "Capillary displacement of viscous liquids in geometries with axial variations," Langmuir **32**, 10513 (2016).
[24]E. M. Benner and D. N. Petsev, "Potential flow in the presence of a sudden expansion: Application to capillary driven transport in porous media," Phys. Rev. E **87**, 033008 (2013).
[25]W. W. Liou, Y. Peng, and P. E. Parker, "Analytical modeling of capillary flow in tubes of nonuniform cross section," J. Colloid Interface Sci. **333**, 389 (2009).
[26]H. Mehrabian, P. Gao, and J. J. Feng, "Wicking flow through microchannels," Phys. Fluids **23**, 122108 (2011).
[27]R. Masoodi and K. M. Pillai, "Darcy's law-based model for wicking in paper-like swelling porous media," AIChE J. **56**, 2257 (2010).
[28]S. Whitaker, "Flow in porous media I: A theoretical derivation of Darcy's law," Transp. Porous Media **1**, 3–25 (1986).
[29]R. Masoodi, K. M. Pillai, and P. P. Varanasi, "Darcy's law-based models for liquid absorption in polymer wicks," AIChE J. **53**, 2769 (2007).
[30]D. Shou and J. Fan, "Structural optimization of porous media for fast and controlled capillary flows," Phys. Rev. E **91**, 053021 (2015).
[31]G. E. Fridley, "Methods and models to control and predict behavior of two dimensional paper networks for diagnostics," Ph.D. thesis (University of Washington, 2014).
[32]D. Gasperino, T. Baughman, H. V. Hsieh, D. Bell, and B. H. Weigl, "Improving lateral flow assay performance using computational modeling," Annu. Rev. Anal. Chem. **11**, 219–29595992 (2018).
[33]N. Sathishkumar and B. J. Toley, "Development of an experimental method to overcome the hook effect in sandwich-type lateral flow immunoassays guided by computational modelling," Sens. Actuators, B **324**, 128756 (2020).
[34]G. Huang, X. Wei, Y. Gu, Z. Kang, L. Lao, L. Li, J. Fan, and D. Shou, "Heterogeneously engineered porous media for directional and asymmetric liquid transport," Cell Rep. Phys. Sci. **3**, 100710 (2022).
[35]E. Elizalde, R. Urteaga, and C. L. A. Berli, "Rational design of capillary-driven flows for paper-based microfluidics," Lab Chip **15**, 2173 (2015).
[36]D. Shou, L. Ye, J. Fan, K. Fu, M. Mei, H. Wang, and Q. Chen, "Geometry-induced asymmetric capillary flow," Langmuir **30**, 5448 (2014).
[37]See T. Williams, C. Kelley *et al.*, http://gnuplot.sourceforge.net/ for "Gnuplot 5.0 patchlevel 5: An interactive plotting program" (2016).
[38]L. Hecht, D. van Rossum, and A. Dietzel, "Femtosecond-laser-structured nitrocellulose membranes for multi-parameter point-of-care tests," Microelectron. Eng. **158**, 52 (2016).
[39]J. Bico and D. Quéré, "Precursors of impregnation," Europhys. Lett. **61**, 348 (2003).
[40]J. Schindelin, I. Arganda-Carreras, E. Frise, V. Kaynig, M. Longair, T. Pietzsch, S. Preibisch, C. Rueden, S. Saalfeld, B. Schmid, J.-Y. Tinevez, D. J. White, V. Hartenstein, K. Eliceiri, P. Tomancak, and A. Cardona, "Fiji: An open-source platform for biological-image analysis," Nat. Methods **9**, 676 (2012).
[41]D. Erickson, D. Li, and C. Park, "Numerical simulations of capillary-driven flows in nonuniform cross-sectional capillaries," J. Colloid Interface Sci. **250**, 422 (2002).
[42]S. Hong and W. Kim, "Dynamics of water imbibition through paper channels with wax boundaries," Microfluid. Nanofluid. **19**, 845 (2015).
[43]J. Tirapu-Azpiroz, A. F. Silva, M. E. Ferreira, W. F. L. Candela, P. W. Bryant, R. L. Ohta, M. Engel, and M. B. Steiner, "Modeling fluid transport in two-dimensional paper networks," J. Micro/Nanolithogr., MEMS, MOEMS **17**, 025003 (2018).
[44]E. Fu, S. A. Ramsey, P. Kauffman, B. Lutz, and P. Yager, "Transport in two-dimensional paper networks," Microfluid. Nanofluid. **10**, 29 (2011).
[45]W. R. Inc., *Mathematica, Version 11.3* (W. R. Inc., Champaign, IL, 2018).
[46]N. Brandt, L. Griem, C. Herrmann, E. Schoof, G. Tosato, Y. Zhao, P. Zschumme, and M. Selzer, "Kadi4Mat: A research data infrastructure for materials science," Data Sci. J. **20**, 8 (2021).
[47]F. Jamshidi, W. Kunz, P. Altschuh, M. Bremerich, R. Przybylla, M. Selzer, and B. Nestler (2022). "Source data belonged to 'Geometric flow control in lateral flow assays: Macroscopic single-phase modeling,'" Zenodo. https://doi.org/10.5281/zenodo.6389659
[48]G. Løvoll, Y. Méheust, K. J. Måløy, E. Aker, and J. Schmittbuhl, "Competition of gravity, capillary and viscous forces during drainage in a two-dimensional porous medium, a pore-scale study," Energy **30**, 861 (2005).
[49]Y. Çengel and J. Cimbala, *Fluid Mechanics: Fundamentals and Applications*, 4th ed. (McGraw-Hill Education, 2018).
[50]K. Li, D. Zhang, H. Bian, C. Meng, and Y. Yang, "Criteria for applying the Lucas-Washburn law," Sci. Rep. **5**, 14085 (2015).